ION CHANNELS, TRANSPORTERS

Rieko Sakai · Claudia Elfgang · Rolf Vogel ·
Klaus Willecke · Robert Weingart

The electrical behaviour of rat connexin46 gap junction channels expressed in transfected HeLa cells

Abstract Pairs of human HeLa cells expressing rat connexin46 were used to study the electrical properties of gap junction channels with the dual voltage-clamp method. The steady-state conductance ($g_{j,ss}$) had a bell-shaped dependence on transjunctional voltage (V_j). The parameters of the Boltzmann fit were: $V_{j,0}$=42 mV, $g_{j,min}$=0.12, z=2.5 (pipette solution: K^+ aspartate$^-$; 27 °C). The Boltzmann parameters were sensitive to the ionic composition of the pipette solution (KCl, K^+ aspartate$^-$, TEA^+ Cl$^-$, TEA^+ aspartate$^-$). The V_j-dependent inactivation of the junctional current I_j was approximated by single exponentials (exceptions: two exponentials with KCl at $V_j \geq 75$ mV and K^+ aspartate$^-$ at V_j=125 mV). The time constant of inactivation (τ_i) decreased with increasing V_j and was sensitive to the pipette solution. The larger the ions, the slower the inactivation. Recovery from inactivation followed a single exponential. The time constant of recovery (τ_r) increased with increasing V_j. Single-channel currents showed a main state, several substates and a residual state. The corresponding conductances $\gamma_{j,main}$ and $\gamma_{j,residual}$ decreased slightly with increasing V_j; extrapolation to V_j=0 mV yielded values of 152 and 28 pS, respectively (K^+ aspartate$^-$; 37 °C). The values of $\gamma_{j,main}$ and $\gamma_{j,residual}$ were dependent on pipette solution. The ratio $\gamma_{j,main}/\gamma_{j,residual}$ increased with increasing ionic size, suggesting that the residual state impairs ion permeation more severely than the main state. The $\gamma_{j,main}$ data suggest that the ionic selectivity of Cx46 channels may be controlled primarily by ionic size. Compared with hemichannel results, docking of connexons may modify the channel structure and thereby affect the ionic selectivity of gap junction channels. The open channel probability at steady state (P_o) decreased with increasing V_j. The parameters of the Boltzmann fit were: $V_{j,0}$=41 mV, z=2.2 (K^+ aspartate$^-$; 27 °C).

Keywords Gap junction · Connexin46 · Electrical properties · Conductance · Kinetics · Lens

R. Sakai · R. Weingart (✉)
Department of Physiology, University of Bern,
Bühlplatz 5, 3012 Bern, Switzerland
e-mail: weingart@pyl.unibe.ch
Tel.: +41-31-6318706
Fax: +41-31-6314611

R. Sakai
Brain Science Institute,
The Institute of Physical and Chemical Research (RIKEN),
Wako-shi, 351-0198 Saitama, Japan

C. Elfgang · K. Willecke
Institute of Genetics, University of Bonn,
53117 Bonn, Germany

R. Vogel
Cardiology, Swiss Cardiovascular Centre Bern,
University Hospital, Inselspital, 3008 Bern, Switzerland

Introduction

The lens of the vertebrate eye consists of a core of regularly packed fibre cells and a layer of epithelial cells covering the anterior surface of the organ. A unique feature of this organ is the absence of a vascular system. To maintain tissue homeostasis, the lens relies on metabolic co-operation via gap junctions. Extensive communication via gap junctions exists between the epithelial cells, between the fibre cells and between the two cell types. This has been documented by morphological and functional studies (see [12]). Immunolocalization and molecular biology techniques have identified three gap junction proteins in the lens, the connexins Cx43, Cx46 and Cx50. While epithelial cells express Cx43 [2, 20], fibre cells produce Cx46 and Cx50 [21, 36].

Functional aspects of Cx46 and Cx50 gap junctions have already been examined in pairs of *Xenopus* oocytes injected with rodent mRNA and information obtained on the voltage sensitivity of the gap junction conductance [11, 36, 37]. However, large membrane current noise has prevented the characterization of single channels. To circumvent this problem, attempts have been made to isolate cell pairs from rodent lenses using enzymatic treatments. While this approach has been successful for

epithelial cells [8], difficulties have been experienced with fibre cells [9]: co-expression of two connexins renders it difficult to determine the electrical properties of identified gap junction channels.

The aim of this study was to explore the electrical properties of Cx46 gap junction channels in HeLa cells transfected with cDNA coding for rat Cx46. The experiments were carried out on cell pairs with variable intercellular coupling. Multi-channel and single-channel currents were recorded under different ionic conditions and the conductive and kinetic properties determined. Preliminary data have been published elsewhere in abstract form [22].

Materials and methods

Cells and culture conditions

Experiments were performed with a clone of human HeLa cells transfected with a cDNA construct containing the coding sequence of rat Cx46. The 1592-bp EcoRI fragment of rat Cx46 cDNA [21] was ligated into the expression vector pBEHpac18 [15] that contained the SV40 early promoter, a polyadenylation signal and a gene conferring resistance to puromycin. In the Cx46 cDNA fragment all ATG codons upstream of the start codon had been removed. HeLa cells were transfected with 20 µg recombinant connexin46-pBEHpac18 plasmid using the calcium phosphate transfection protocol [6]. Between 24 and 48 h after exposure to DNA, the antibiotic puromycin (1 µg/ml) was added to the medium. Clones were selected after 3 weeks, grown in DMEM (Gibco, Paisley, UK) containing 10% FCS and 1 µg/ml puromycin (Sigma, St. Louis, MO, USA), passaged weekly and diluted 1:10. For experiments, monolayers of cells (~4×10^5 cells/cm^2) were harvested and re-suspended in DMEM containing 10% FCS (0.2–1×10^6 cells/ml). Thereafter, the cells were seeded onto sterile glass cover-slips (~10^4 cells/cm^2) placed in multi-well culture dishes and used within 24 h after plating.

Solutions

Experiments were carried out in modified Krebs-Ringer solution (mM): NaCl 150, KCl 4, $CaCl_2$ 2, $MgCl_2$ 1, glucose 5, pyruvate 2, HEPES 5 (pH 7.4). Patch pipettes were filled with normal pipette solution (in mM): K^+ aspartate$^-$ 120, NaCl 10, $MgCl_2$ 1, $CaCl_2$ 1, HEPES 5 (pH 7.2), EGTA 10 (pCa$\cong$8), MgATP 3, through a 0.22-µm-pore filter. In some experiments, K^+ aspartate$^-$ was replaced by equimolar amounts of KCl, TEA^+ Cl^- or TEA^+ aspartate$^-$. The specific conductance of the pipette solutions was determined with a conductivity meter (CDM 83; Radiometer, Copenhagen, Denmark) at 27 °C.

Electrical measurements

Cover-slips with adherent cells were transferred to a chamber superfused at 2 ml/min with saline at 27 °C. To alter the temperature, saline reservoirs were kept in heated or cooled vessels. The temperature in the chamber was measured with a thermistor positioned close to the cells. The chamber was mounted on the stage of an inverted microscope equipped with phase-contrast optics (Diaphot-TMD, Nikon; Nippon Kogaku, Tokyo, Japan). Patch pipettes were pulled from glass capillaries (GC150F-10; Harvard Apparatus, Edenbridge, UK) using a horizontal puller (DMZ-Universal; Zeitz Instruments, Munich, Germany). When filled with solution, they had DC resistances of 3–6 MΩ. Experiments were carried out on cell pairs formed in culture [28]. Each

cell of a pair was attached to a pipette. After establishing a GΩ-seal, the membrane patch was disrupted enabling whole-cell recording. The pipettes were connected to separate amplifiers (EPC7; List Electronic, Darmstadt, Germany). A dual voltage-clamp method allowed the membrane potential of each cell to be controlled (V_1, V_2) and the current flow through each pipette to be measured (I_1, I_2). Initially, the membrane potential of both cells was clamped to −30 mV. Thereafter, a junctional voltage (V_j) was established by de- or hyperpolarizing cell 1 while maintaining the membrane potential of cell 2. Under these conditions, V_j corresponds to the voltage between the cells, $V_j=V_2-V_1$. The current recorded from cell 1 represents the sum of two components, a gap junction current (I_j) and a non-junctional membrane current ($I_{m,1}$), the current recorded from cell 2 is thus −I_j. Voltage and current signals were stored on FM tape (SE 3000; SE Lab, Feltham, UK). For analysis the signals were filtered at 1 kHz (8-pole Bessel filter) and digitized at 2 kHz (12-bit A/D converter IDA 12120; INDEC Systems, Capitola, Calif., USA). Data acquisition and analysis were performed with the software C-Lab (INDEC Systems). Curve fitting and statistical analysis were done with SigmaPlot and SigmaStat, respectively (Jandel Scientific, Erkrath, Germany). The results are presented as means±SEM. The significance of differences between means was established using Student's t-test.

Biophysical modelling

Electrical properties of gap junction channels were modelled by two different approaches. The first method relies on macroscopic data and uses a top-down algorithm by assuming hemichannel properties (VW-model) [33]. The second method uses a bottom-up algorithm such as the Poisson-Nernst-Planck formulation of electrodiffusion, which is based on the combined treatment of selectivity and permeation (PNP-model) [7]. This model has been applied previously to describe the properties of single ion channels [7] as well as single gap junction channels and hemichannels [24]. It considers local chemical interactions depicted by an offset in chemical potential, which probably reflects differences in dehydration, solvation and rehydration energies associated with entry and exit steps of channel permeation. These interactions are modelled by fixed charges distributed along the channel. The purpose of the latter simulation is to demonstrate that specific charge profiles are able to reproduce the essential features of Cx46 single-channel conductance. However, it would have been beyond the scope of the present work to derive a set of parameters representing the best fit to the problem. I/V-curves were calculated using the code solving the PNP equation available at http://www.pnponline.org./program.php. The PNP solver is accessed via a graphical user interface. The settings of the PNP parameters were as follows: pore length=100 Å, left ion concentration=120 mM, right ion concentration=120 mM, diffusion coefficient of cation=2.048×10^{-5} cm^2/s (K^+), diffusion coefficient of anion=0.655×10^{-5} cm^2/s (aspartate$^-$), ambient temperature=27 °C, relative dielectric constant of aqueous pore=80. For the comparison with biological data, the I/V-curves were transformed into conductance/voltage curves.

Results

Voltage dependence of gap junction currents

Voltage pulses of long duration (10 s), variable amplitude (≤150 mV) and either polarity were applied to one cell of the pair while the junctional current I_j was recorded from the other. Figure 1A shows records obtained with the pipette solution containing K^+ aspartate$^-$ as major charge carriers. Hyperpolarization of cell 2 by 75 mV (V_2, left-hand side) provoked an I_j with time-dependent inactiva-
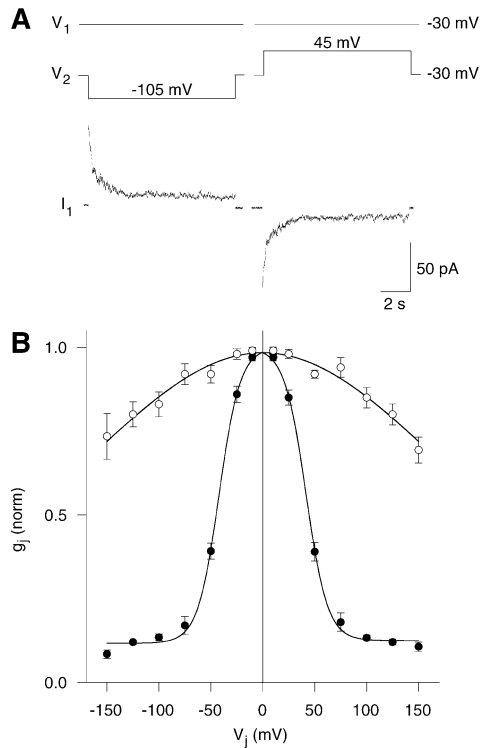
Fig. 1A, B Dependence of the multi-channel currents I_j on transjunctional voltage V_j in pairs of HeLa cells expressing rat connexin Cx46 gap junctions. **A** Responses of I_j to V_j. V_1, V_2: membrane potential of cell 1 and cell 2; I_1: current measured from cell 1. *Deflections* in V_2 and I_1 correspond to V_j and I_j, respectively. $V_j=\pm75$ mV. **B** Normalized gap junction conductance, $g_j(norm)$, determined at the beginning ($g_{j,inst}$; ◯) and end ($g_{j,ss}$; ●) of V_j pulses, as a function of V_j (ten cell pairs). The *curves* $g_{j,inst}=f(V_j)$ and $g_{j,ss}=f(V_j)$ show the best fits to Eqs. 1 and 2, respectively. For the Boltzmann parameters, see Table 1

tion (I_1, left-hand side). Depolarization of the same magnitude led to a similar I_j of opposite polarity (V_2 and I_1, right-hand side). To perform a complete experiment, the transjunctional voltage V_j was altered stepwise between ±10 and ±150 mV. Figure 1B summarizes the results from ten cell pairs. The amplitude of I_j was determined at the beginning ($I_{j,inst}$; inst: instantaneous) and end ($I_{j,ss}$; ss: steady state) of each V_j pulse to calculate the conductances $g_{j,inst}=I_{j,inst}/V_j$ and $g_{j,ss}=I_{j,ss}/V_j$, respectively. On the one hand, the values of $g_{j,inst}$ were normalized with respect to the maximal $g_{j,inst}$ at small V_j gradients. The normalized values of $g_{j,inst}$ were plotted as a function of V_j ($g_{j,inst}=f(V_j)$, open circles). On the other hand, the values of $g_{j,ss}$ were normalized with respect to the $g_{j,inst}$ prevailing at each V_j. The normalized $g_{j,ss}$ were plotted as a function of V_j ($g_{j,ss}=f(V_j)$, solid circles). Cell pairs with $g_{j,inst}>2$ nS were excluded from the analysis to minimize series resistance problems [3, 35].

The $g_{j,inst}$ data exhibited a slight curvature with a symmetry at $V_j=0$ mV. The smooth curve represents the best fit of data to:

Table 1 Electrical properties of multi-channel gap junction currents. Means±SEM (in parentheses) for negative/positive transjunctional potential V_j ($g_{j,min}$ is the normalized conductance at large V_j

Pipette solutions	$V_{j,0}$ (mV)	$g_{j,min}$	z	n
KCl	−32.4/30.4 (1.1/1.6)	0.15/0.15 (0.01/0.02)	2.6/2.7 (0.2/0.3)	10
K^+ aspartate$^-$	−42.1/41.6 (0.5/0.7)	0.12/0.12 0.01/0.01	2.5/2.5 (0.1/0.1)	10
TEA^+ Cl^-	−45.7/44.0 (0.6/0.5)	0.10/0.10 (0.01/0.01)	2.2/2.5 (0.1/0.1)	9
TEA^+ aspartate$^-$	−45.1/45.2 (0.5/0.6)	0.07/0.07 (0.01/0.01)	2.4/2.3 (0.1/0.1)	7

The following differences were not significant statistically (Student's *t*-test): $V_{j,0}$ data: TEA^+ Cl^- vs. TEA^+ aspartate$^-$; z data: KCl vs. K^+ aspartate$^-$, K^+ aspartate$^-$ vs. TEA^+ Cl^-, TEA^+ Cl^- vs. TEA^+ aspartate$^-$

$$g_{j,inst} = \frac{G_j}{e^{V_H\left(1+e^{\frac{V_j}{V_H}}\right)} + e^{V_H\left(1+e^{\frac{-V_j}{V_H}}\right)}} \tag{1}$$

(VW-model; Eq. 29 in [33]). G_j is a dimensionless fitting parameter and V_H a decay constant. The analysis yielded the following values: $G_j=2.0$; $V_H=−159$ mV. At $V_j=0$ mV $g_{j,inst}$ was 1.0 and 0.85 at $V_j=\pm100$ mV.

The $g_{j,ss}$ data followed a bell-shaped relationship which was nearly symmetrical. At $V_j=0$ mV, $g_{j,ss}$ was maximal. Between $V_j=\pm15$ and ±75 mV, it decreased steeply. Beyond ±100 mV, it remained virtually constant. The smooth curve represents the best fit of data to the Boltzmann equation applied separately to each voltage polarity:

$$g_{j,ss} = \frac{1-g_{j,min}}{1+e^{\left[A\left(V_j-V_{j,0}\right)\right]}} + g_{j,min} \tag{2}$$

where $g_{j,min}$ is the normalized conductance at large V_j and $V_{j,0}$ corresponds to the V_j at which $g_{j,ss}/g_{j,inst}$ is half-maximally inactivated. A is a constant expressing gating charge, $zq(kT)^{-1}$ [13]. The values obtained from the analysis are given in Table 1 (pipette solution: K^+ aspartate$^-$).

The voltage dependence of I_j was also examined in the presence of pipette solutions containing KCl, TEA^+ Cl^- or TEA^+ aspartate$^-$ as major charge carriers (signals not shown). The records obtained indicated distinct differences in V_j sensitivity of I_j. Figure 2 shows the results of the analysis plotting the normalized $g_{j,ss}$ vs. $f(V_j)$ for the three solutions: KCl (circles, solid curve); TEA^+ Cl^-(squares, dashed curve); TEA^+ aspartate$^-$ (triangles; dotted curve). The smooth curves represent the best fit of data to the Boltzmann equation. The values obtained from the analysis are given in Table 1. A comparison of the data indicates subtle differences caused by the ions of the pipette solutions.
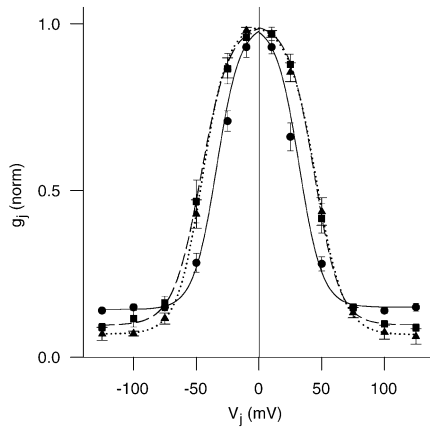
Fig. 2 Effects of intracellular ions on the dependence of I_j on V_j. The cells were dialysed with pipette solutions containing KCl (●), TEA$^+$ Cl$^-$ (■) or TEA$^+$ aspartate$^-$ (▲) as major charge carriers. The normalized gap junction conductance at steady state, $g_{j,ss}$, is plotted vs. V_j; n=10, 9 and 7 cell pairs, respectively. The *curves* show the best fits to Eq. 2. *Solid curve*: KCl; *dashed curve*: TEA$^+$ Cl$^-$; *dotted curve*: TEA$^+$ aspartate$^-$. For the Boltzmann parameters, see Table 1
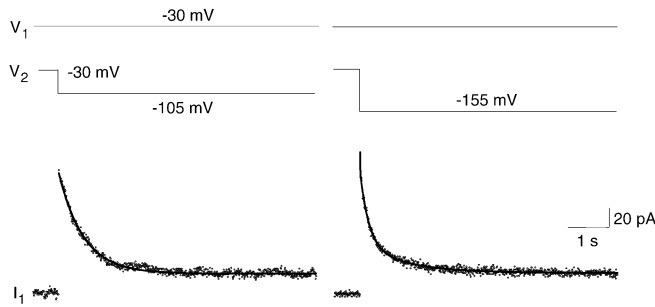
Fig. 3 Influence of V_j on the time course of I_j inactivation. Current traces I_1 obtained at V_j=−75 mV (*left*) and −125 mV (*right*). The *smooth curves* are the best fits of currents to Eqs. 3 and 4

Inactivation of gap junction currents

Next we explored the kinetics of I_j inactivation using pipette solution with K$^+$ aspartate$^-$. Figure 3 shows signals gained at V_j=−75 mV (left-hand panel) and V_j=−125 mV (right-hand panel). The velocity of I_j inactivation was sensitive to the amplitude of V_j, with acceleration as V_j increased. To analyse the time course of inactivation, I_j signals were subjected to least-squares curve fitting. At V_j=−75 mV, the best fit was achieved with a single exponential:

$$I_j(t) = I_{j1} \cdot e^{-\left(\frac{t}{\tau_{i1}}\right)} + I_{j,ss} \tag{3}$$

where $I_j(0)$ corresponds to I_j at time t=0 and equals $I_{j1}+I_{j,ss}$; τ_{i1} is the time constant of I_j inactivation. At V_j=−125 mV, the sum of two exponentials provided a better fit:

$$I_j(t) = I_{j1} \cdot e^{-\left(\frac{t}{\tau_{i1}}\right)} + I_{j2} \cdot e^{-\left(\frac{t}{\tau_{i2}}\right)} + I_{j,ss} \tag{4}$$
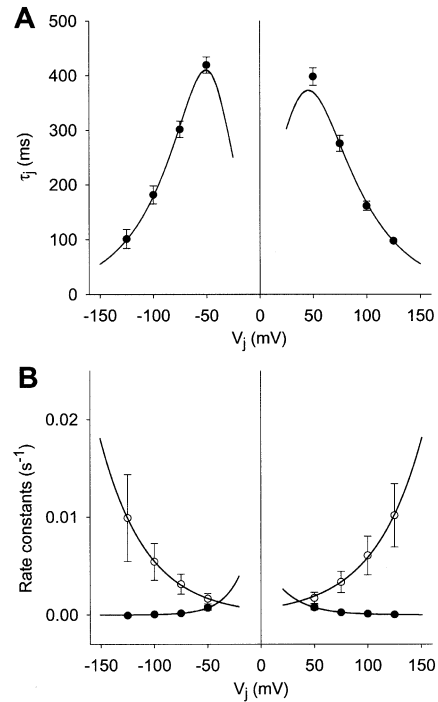
Fig. 4A, B Kinetic properties of I_j inactivation. **A** Plot of time constants of I_j inactivation, τ_{i1}, as functions of V_j. Data from ten cell pairs. The curves were calculated from Eq. 9 taking into account the values for α and β determined by Eqs. 7 and 8. **B** The rate constants of channel opening, α (●), and closing, β (○) as functions of V_j. The *curves* show the best fits to Eqs. 7 and 8. For the kinetic parameters obtained, see Table 2

In this case, $I_j(0)$ equals $I_{j1}+I_{j2}+I_{j,ss}$. The smooth curves indicate the best fit of I_j to Eqs. 3 and 4, respectively. The analysis yielded the following values: τ_{i1}=240 ms (V_j=−75 mV); τ_{i1}=83 ms, τ_{i2}=438 ms (V_j=−125 mV). In the latter case, τ_{i1} and τ_{i2} were different by a factor of 5.3, suggesting that this phenomenon is genuine.

Figure 4A summarizes the inactivation data from ten cell pairs. The values of τ_i were obtained from individual I_j records, averaged and plotted as a function of V_j. For V_j up to ±100 mV, the analyses yielded single time constants, τ_{i1}, for larger values of V_j, fitting with two time constants was more appropriate, τ_{i1} and τ_{i2}. The symbols correspond to mean values of τ_{i1} (τ_{i2} omitted for clarity). The values at V_j of 25 mV were rejected due to the small I_j amplitude and the poor signal/noise ratio. Over the voltage range analysed, τ_{i1} decreased with increasing V_j for both polarities.

Considering a two-state process (main state ⇆ residual state; see Single-channel conductances), the rate constants for channel opening (α) and closing (β) can be estimated according to [13]:

$$\alpha = \frac{\frac{g_{j,ss}(V_j)}{g_{j,inst}(V_j)} - g_{j,min}}{\left(1 - g_{j,min}\right) \cdot \tau_i} \tag{5}$$

and
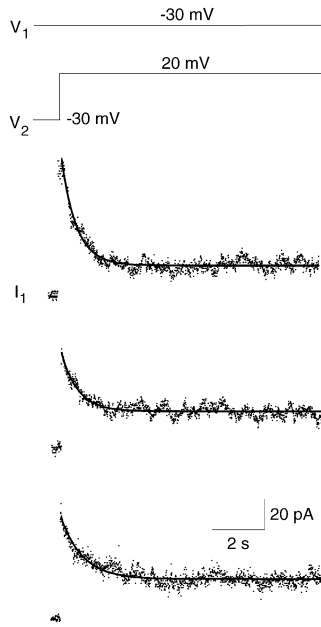
Fig. 5 Influence of pipette solution on the time course of I_j inactivation. I_j records were obtained with pipette solutions containing KCl (*top*), TEA$^+$ Cl$^-$ (*middle*) and TEA$^+$ aspartate$^-$ (*bottom*). V_j=50 mV (V_1=−80 mV, V_2=−30 mV), pulse duration=10 s. The analyses yielded single time constants. The *smooth curves* are the best fits of currents to Eq. 3

$$\beta = \frac{1 - \frac{g_{j,ss}(V_j)}{g_{j,inst}(V_j)}}{\left(1 - g_{j,min}\right) \cdot \tau_i} \tag{6}$$

Using these equations, values for α and β were calculated from the data in Fig. 4A and plotted as functions of V_j (Fig. 4B). The graphs α=$f(V_j)$ (solid circles) and β=$f(V_j)$ (open circles) indicate that τ_i is governed by α at low V_j and by β at large V_j. The smooth curves represent the best fit of data to:

$$\alpha = \lambda \cdot e^{\left[-A_\alpha\left(V_j - V_{j,0}\right)\right]} \tag{7}$$

and

$$\beta = \lambda \cdot e^{\left[A_\beta\left(V_j - V_{j,0}\right)\right]} \tag{8}$$

where A_α and A_β express the voltage sensitivity of the rate constants and λ is a constant corresponding to the rate at which α=β (prevails at V_j=$V_{j,0}$) [13]. The analysis yielded similar values for negative/positive V_j: λ=0.0013/ 0.0014 s^{-1}; A_α=−0.058/0.042 mV^{-1}; A_β=−0.024/ 0.022 mV^{-1}; $V_{j,0}$=−40.2/36.5 mV. It follows that β>α when V_j>$V_{j,0}$ and β<α when V_j<$V_{j,0}$. The combination of Eqs. 7 and 8 enables τ_{i1} to be calculated:

$$\tau_{i1} = \frac{1}{\alpha + \beta} \tag{9}$$

This relationship was used to plot the function τ_{i1}=$f(V_j)$ for negative and positive V_j (continuous lines in Fig. 4A). The resulting curves show a maximum at V_j≅50 mV. There is a reasonable correlation between the curves and
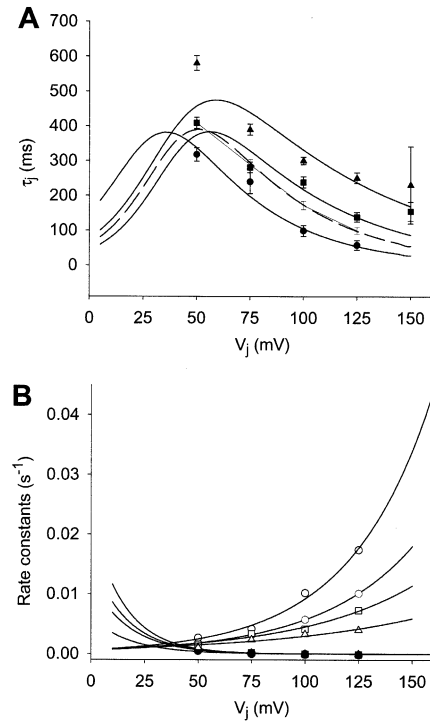
Fig. 6A, B Effects of intracellular ions on kinetic properties of I_j inactivation. **A** Time constants of I_j inactivation, τ_i, as functions of V_j. Values of τ_{i1} obtained at negative and positive V_j were pooled and averaged (● KCl, n=10; ■ TEA$^+$ Cl$^-$ n=9; ▲ TEA$^+$ aspartate$^-$ n=7). The *smooth curves* were calculated from Eq. 9. The *dashed curve* shows the K$^+$ aspartate$^-$ data from Fig. 4A after pooling. **B** Rate constants of channel opening, α (*solid symbols*) and channel closure, β (*open symbols*), deduced from the time constants in **A**, as functions of V_j. The *smooth curves* show the best fits to Eqs. 7 and 8. The *dashed curve* shows the K$^+$ aspartate$^-$ data from Fig. 4B after pooling. For the kinetic parameters obtained, see Table 2

the experimentally determined values of τ_{i1} over the voltage range examined, i.e. V_j=±50 to ±125 mV.

The kinetics of I_j inactivation were also studied in the presence of other pipette solutions. Figure 5 shows current records obtained with KCl (top), TEA$^+$ Cl$^-$ (middle) and TEA$^+$ aspartate$^-$ (bottom). V_j pulses of 50 mV amplitude and 10 s duration were used (V_1=−30 mV, V_2=−80 mV). In the case of KCl, TEA$^+$ Cl$^-$ and TEA$^+$ aspartate$^-$, inactivation followed a single exponential with a τ_{i1} of 333, 417 and 500 ms, respectively (smooth curves). Hence, inactivation of I_j was affected by the ions of the pipette solution. Figure 6 summarizes the data obtained with these solutions (KCl: n=10; TEA$^+$ Cl$^-$: n=9; TEA$^+$ aspartate$^-$: n=7). The time constants extracted were sampled, averaged and plotted on a logarithmic scale as a function of V_j (Fig. 6A). Negative and positive V_j yielded similar τ_i values and hence were pooled. In the case of TEA$^+$ Cl$^-$ (squares) and TEA$^+$ aspartate$^-$ (triangles), a single time constant was obtained at each V_j. In the case of KCl (circles), a single time constant was found at V_j=50 mV and two at V_j≥75 mV (for clarity, only τ_{i1} is shown). The different pipette solutions gave rise to

Table 2 Inactivation parameters of multichannel gap junction currents. Values of λ, $V_{j,0}$, A_α and A_β were deduced from the data in Fig. 6B (λ constant corresponding to the rate at which $\alpha=\beta$, i.e. at $V_j=V_{j,0}$, α, β rate constants of channel opening and closure, respectively, A_α, A_β voltage sensitivity of the respective rate constants)

| Pipette solutions	λ (s^{-1})	$V_{j,0}$ (mV)	A_α (mV^{-1})	A_β (mV^{-1})
KCl	0.0014	26.5	0.056	0.026
K^+ aspartate$^-$	0.0014	39.3	0.062	0.023
TEA^+ Cl^-	0.0015	41.2	0.065	0.019
TEA^+ aspartate$^-$	0.0013	39.0	0.058	0.014

distinct relationships between τ_{i1} and V_j. In each case, τ_{i1} decreased with increasing V_j.

Equations 5 and 6 were then used to calculate the rate constants α and β for the different pipette solutions. Figure 6B shows the resulting plots. Solid and open symbols correspond to α and β, respectively. The solid curves represent the best fit of data to Eqs. 7 and 8. The fitting parameters obtained from the analysis are summarized in Table 2. For comparison, Fig. 6B and Table 2 also include the kinetic data for K^+ aspartate$^-$ solution already shown in Fig. 4B (dashed curves, symbols omitted). This involved pooling of the values for positive and negative V_j. According to Fig. 6B, $\beta=f(V_j)$ increased with increasing V_j while $\alpha=f(V_j)$ decreased. The increase in β was dependent on the ionic composition of the pipette solution. The smaller the ions, the more pronounced the effect. In contrast, the decrease in α was virtually insensitive to the ions. Hence, the increase in τ_{i1} brought about by the substitution of KCl for TEA^+ aspartate$^-$ can be explained with an increase in β.

The rate constants gained for KCl, TEA^+ Cl^- and TEA^+ aspartate$^-$ were then used to calculate τ_{i1} as a function of V_j using Eq. 9. The continuous curves in Fig. 6A illustrate the results. The function $\tau_{i1}=f(V_j)$ for K^+ aspartate$^-$, already shown in Fig. 4A, are also included (dashed curve, symbols omitted). For this purpose, the data for negative and positive V_j were pooled. The graph shows a distinct correlation between τ_{i1} and the ions of the pipette solution for voltages larger than 50 mV. The solutions containing the smallest ions, i.e. KCl, gave rise to the smallest τ_{i1} values, the solution with the largest ions, i.e. K^+ aspartate$^-$, gave rise to the largest τ_{i1} values.

Recovery of I_j from inactivation

We have also examined the recovery of I_j from inactivation using pipette solution with K^+ aspartate$^-$. The upper panel in Fig. 7A shows the pulse protocol. A conditioning pulse applied to cell 1 (pulse 1) was followed by a test pulse (pulse 2) after a variable delay. Both pulses produced a V_j of 100 mV amplitude and 5 s duration. They allowed I_j to inactivate maximally and reach a steady state. The lower panel shows superimposed traces indicating that $I_{j,inst}$ of pulse 2 grew larger with increasing inter-pulse interval. To examine the role of V_j
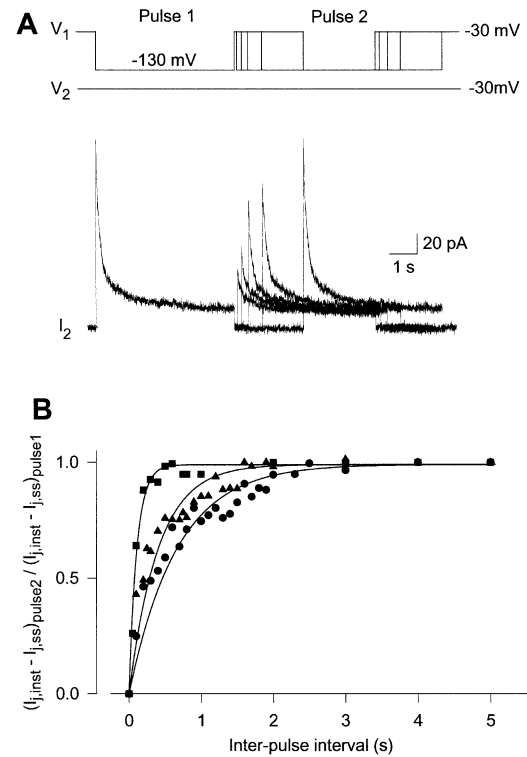

Fig. 7A, B Recovery of I_j from inactivation. **A** Double pulse protocol used to determine I_j associated with a test pulse (*pulse 2*) applied at different times after a conditioning pulse (*pulse 1*). V_1, V_2: superimposed membrane potentials of cells 1 and 2; I_2: family of current traces from cell 2. *Deflections* in V_1 and I_2 correspond to V_j and I_j, respectively. **B** $(I_{j,inst}-I_{j,ss})_{pulse2}/(I_{j,inst}-I_{j,ss})_{pulse1}$ as a function of inter-pulse interval. Data were obtained at $V_j=50$ mV (■; 5 cell pairs), 75 mV (▲; 11 cell pairs) and 100 mV (●; 8 cell pairs). The *smooth curves* are the best fits to Eq. 10

on I_j recovery, we also used pulses of different amplitude (traces not shown). Figure 7B summarizes the results obtained. For each pulse, the current inactivated was calculated, i.e. $I_{j,inst}-I_{j,ss}$. Thereafter, the values of $I_{j,inst}-I_{j,ss}$ associated with pulse 2 were normalized relative to $I_{j,inst}-I_{j,ss}$ associated with pulse 1 and plotted as a function of the inter-pulse interval. The data illustrated were obtained at $V_j=50$ mV (squares; $n=5$), 75 mV (triangles; $n=11$) and 100 mV (circles; $n=8$). The smooth curves correspond to the best fit of data to a single exponential:

$$\frac{(I_{j,inst}-I_{j,ss})_{pulse2}}{(I_{j,inst}-I_{j,ss})_{pulse1}} = 1 - \left(e^{\left(\frac{t}{\tau_r}\right)}\right) \tag{10}$$

where τ_r is the time constant of recovery and t the inter-pulse interval. The analysis yielded the following values for τ_r: $V_j=100$ mV: 662 ms; $V_j=75$ mV: 404 ms; $V_j=50$ mV: 111 ms. Hence, the larger the inactivation of I_j, the slower the recovery.
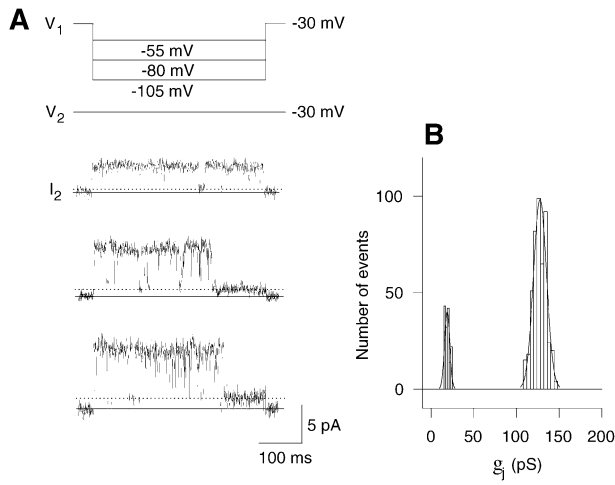
Fig. 8A, B Single-channel currents. **A** Responses of I_j to $V_j=25$, 50 and 75 mV (I_2 signals from *top* to *bottom*). V_1, V_2: membrane potential of cells 1 and 2; I_2: current measured from cell 2. *Deflections* in V_1 and I_2 correspond to V_j and I_j, respectively. *Continuous lines* indicate zero current, *dotted lines* the residual current. The analysis yielded the following conductances ($\gamma_{j,main}$/$\gamma_{j,residual}$): 136/23 pS; 130/20 pS; 118/18 pS, respectively. **B** Histogram of single-channel conductances. The analysis included values obtained at $V_j=\pm50$ mV (14 cell pairs). The left and right hand distributions reflect $\gamma_{j,residual}$ and $\gamma_{j,main}$ data, respectively. The *smooth curves* show the best fits to Gaussian functions. For the values obtained, see Table 3

Single-channel conductances

Single-channel events were studied in cell pairs with gap junctions consisting of between one and three operational channels. The protocol involved repetitive application of V_j pulses of 200–500 ms duration, different amplitude (≤100 mV) and either polarity. Figure 8A shows signals using pipette solution with K^+ aspartate$^-$. Hyperpolarization of cell 1 (V_1) led to a V_j of 25, 50 and 75 mV. The associated I_j signals (I_2 traces from top to bottom) showed discrete levels corresponding to the main state, the residual state (dotted lines) and short-lived substates in between. During V_j pulses, I_j did not return to the reference level (solid lines) indicating that the channels failed to close completely. The analysis yielded the following conductances ($\gamma_{j,main}$/$\gamma_{j,residual}$): 136/23, 130/20 and 118/18 pS, for V_j of 25, 50 and 75 mV, respectively.

The histograms in Fig. 8B summarize the results from 14 cell pairs plotting the number of events vs. conductance. The values of $\gamma_{j,residual}$ and $\gamma_{j,main}$ were pooled in 2- and 4-pS bins, respectively. To avoid interference from the sensitivity to V_j (see below), this analysis included data at $V_j=\pm50$ mV only. The left- and right-hand distributions correspond to $\gamma_{j,residual}$ and $\gamma_{j,main}$, respectively. Both data sets showed a binomial distribution approximated by a Gaussian function (smooth curves). The mean values of $\gamma_{j,main}$ and $\gamma_{j,residual}$ were 127.5±0.4 pS ($n=471$) and 19.0±0.3 pS ($n=175$), respectively.

To assess the relationships between V_j and γ_j, I_j records gained at different V_j were considered. Values of $\gamma_{j,main}$
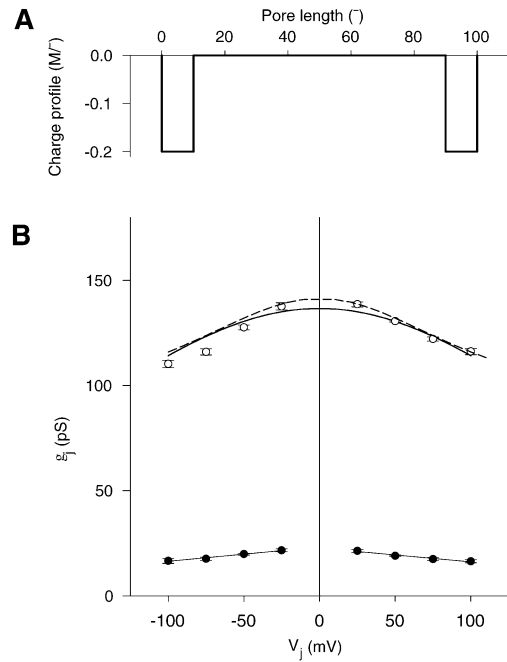

Fig. 9A, B Relationship between single-channel conductances, γ_j, and V_j. Comparison of simulations by the VW- and PNP-models. **A** Charge density profile of the PNP-model. The graph shows two negative charge regions (2 mol/l) located at the pore endings, each occupying 10% of the pore length. **B** Conductances $\gamma_{j,main}$ ($\bigcirc$) and $\gamma_{j,residual}$ ($\bullet$) as functions of V_j (14 cell pairs). Means±SEM, $n=471$ and 175 determinations, respectively. Most *error bars* are smaller than the symbols. The *solid curves* correspond to the relationships $\gamma_{j,main}=f(V_j)$ and $\gamma_{j,residual}=f(V_j)$ and show the best fits to the VW-model. The *dashed curve* shows the $\gamma_{j,main}$ data simulated by the PNP-model, assuming a pore radius of 5.3 Å

and $\gamma_{j,residual}$ were sampled, averaged and plotted as a function of V_j. Figure 9B illustrates the relationships $\gamma_{j,main}=f(V_j)$ (open circles) and $\gamma_{j,residual}=f(V_j)$ (solid circles). $\gamma_{j,main}$ showed a slight dependence on V_j, i.e. it was maximal at $V_j=0$ mV and decreased as V_j was increased. $\gamma_{j,main}$ was fitted to the function:

$$\gamma_{j,main} = \frac{\Gamma_H}{e^{\frac{-V_j}{V_H\left(1+e^{\frac{V_j}{V_H}}\right)}} + e^{\frac{V_j}{V_H\left(1+e^{\frac{-V_j}{V_H}}\right)}}} \quad (11)$$
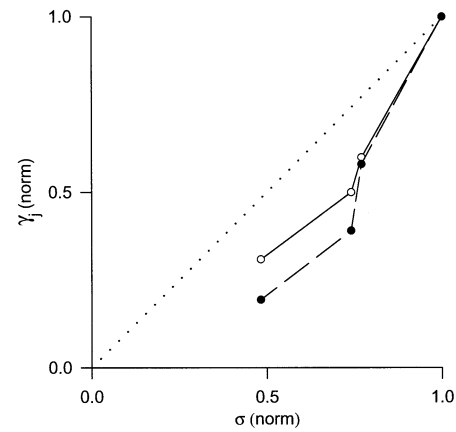
(VW-model; Eq. 29 in [33]). Γ_H is the conductance of a hemichannel in the high-conductance state, i.e. the main state, at $V_j=0$ mV. The analysis yielded the following values: $\Gamma_H=276$ pS; $V_H=-129$ mV. $\gamma_{j,residual}$ also showed a moderate dependence on V_j, i.e. it decreased with increasing V_j. Reliable measurements were obtained for V_j between ±25 and ±100 mV. At $V_j <\pm25$ mV, $\gamma_{j,residual}$ events were rare and too small to be resolved (see below). $\gamma_{j,residual}$ data were fitted using a standard error minimization procedure. The analysis gave the following values: $\Gamma_L=25$ pS, $V_L=-244$ mV. Γ_L represents the conductance of a hemichannel in the low-conductance, i.e. residual, state, at $V_j=0$ mV [33].
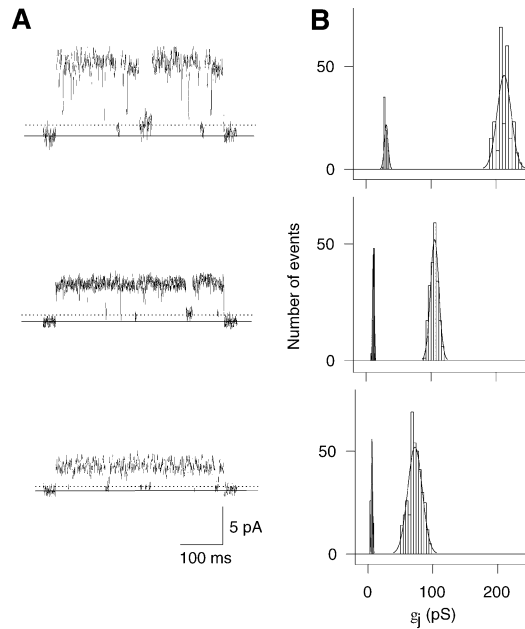
Fig. 10A, B Influence of intracellular ions on single-channel currents. The cells were dialysed with pipette solutions containing KCl (*top*), TEA$^+$ Cl$^-$ (*middle*) and TEA$^+$ aspartate$^-$ (*bottom*) as major charge carriers. **A** Responses of I_j to a V_j pulse of 50 mV and 400 ms (V_1=−80 mV, V_2=−30 mV). *Continuous lines* indicate zero current, *dotted lines* residual current. **B** Histograms of single-channel conductances. The analysis included values obtained at V_j=±50 mV only. The *left-* and *right-hand* distributions reflect $\gamma_{j,residual}$ and $\gamma_{j,main}$ data, respectively. The *smooth curves* show the best fits to Gaussian functions. For the values obtained, see Table 3

Fig. 11 Selective permeability of single channels. Plot of the normalized channel conductances $\gamma_{j,main}$ (○) and $\gamma_{j,residual}$ (●) vs. normalized conductance of the pipette solution, σ. Pipette solution containing KCl was used as reference. The *dotted line* indicates identical ionic mobility in the channel pore and in bulk solution

Table 3 Single-channel conductances (γ_j) for the main and residual conductance states. Means±SEM. *Values* in *parentheses* give the number of cell pairs and the number of observations. Channel conductances were obtained at V_j=50 mV (σ conductance of pipette solution)

Pipette solutions	$\gamma_{j,main}$ (pS)	$\gamma_{j,residual}$ (pS)	σ (mS/cm)
KCl	212.7±0.9 (8/248)	31.5±0.4 (8/71)	17.5
K$^+$ aspartate$^-$	127.5±0.4 (14/471)	19.0±0.2 (14/175)	13.5
TEA$^+$ Cl$^-$	108.8±0.4 (5/209)	12.3±0.1 (5/71)	13.0
TEA$^+$ aspartate$^-$	65.7±0.6 (10/307)	6.1±0.4 (10/75)	8.4

Since a gap junction channel consists of two hemichannels in series, $\gamma_{j,main}$ and $\gamma_{j,residual}$ at V_j=0 mV can be calculated as $\Gamma_H/2$=138 pS and $(\Gamma_H-\Gamma_L)/(\Gamma_H+\Gamma_L)$=23 pS, respectively. Taking into account the values of Q_{10} (see Influence of temperature on gap junction currents), $\gamma_{j,main}$ and $\gamma_{j,residual}$ at 37 °C would be 152 and 28 pS, respectively.

To explore the ionic permeability of Cx46 channels, unitary currents were also recorded with pipette solutions containing KCl, TEA$^+$ Cl$^-$ or TEA$^+$ aspartate$^-$. In the presence of TEA$^+$ aspartate$^-$, I_j records often showed critical signal/noise ratios. In these cases, the currents were analysed using an all-point procedure. Figure 10A shows selected I_j traces elicited by a standard V_j pulse (50 mV, 400 ms). Each trace exhibited two prominent levels attributable to the main and residual states (dotted lines). In the presence of KCl, $\gamma_{j,main}$ and $\gamma_{j,residual}$ were 207 and 33 pS, respectively (top). With TEA$^+$ Cl$^-$, the respective conductances were 108 and 13 pS (middle), with TEA$^+$ aspartate$^-$, 65 and 6 pS (bottom). Hence, $\gamma_{j,main}$ and $\gamma_{j,residual}$ decreased with increasing ionic size of the major charge carriers. Figure 10B summarizes the data. Values of $\gamma_{j,residual}$ and $\gamma_{j,main}$ were sampled in 2- and 4-pS bins, respectively, and plotted as frequency histograms. The two distributions correspond to the $\gamma_{j,residual}$ and $\gamma_{j,main}$ data. The smooth curves represent the best fit of data to a Gaussian function. Table 3 summarizes the results of the analysis and includes the values for K$^+$ aspartate$^-$ (see Fig. 8B).

Figure 11 shows a normalized plot of the channel conductance, γ_j, as a function of the conductance of the pipette solution, σ. The values of γ_j were taken from the experiments described above, the values of σ were measured with a conductivity meter (see Table 3). The KCl pipette solution served as reference. The symbols correspond to $\gamma_{j,main}$ (open circles) and $\gamma_{j,residual}$ data (solid circles). The dotted line represents the function $\sigma=m\cdot\gamma_j$ with m=1, assuming identical ionic mobility in the channel pore and in bulk solution. Neither $\gamma_{j,main}$ nor $\gamma_{j,residual}$ fulfilled this prediction, suggesting interactions between the ions and the channel structure.

Simulations with the PNP-model

For calculations with the PNP-model, the gap junction channel is divided into ten segments of piecewise constant and fixed charges. Segments 1 and 10 include the intracellular endings of the channel, while segments 5

and 6 represent the docking area of the hemichannels. Independent of charge polarity, $\gamma_{j,main}$ increased with increasing $|V_j|$ when charges were fixed near the docking zone, i.e. in segments 4–6 (data not shown). However, the opposite behaviour can be simulated by placing fixed charges of either polarity close to the proximity of the cytosolic channel ending, i.e. in segments 1, 2, 9 and 10.

As determined experimentally, $\gamma_{j,main}$ of a Cx46 channel decreases from about 135 to 110 pS when V_j is increased from 25 to 100 mV (see Fig. 9B). This behaviour can be approximated by the PNP-model when fixed negative charges are placed in segments 1 and 10. Positive charges that produced conductances of the same order are very small and thus the channel conductance becomes almost independent of V_j. The graph in Fig. 9A shows the charge density profile comprising two negatively charged regions (2 mol/l), each occupying 10% of the pore length and located towards the intracellular end. Figure 9B includes the result of the respective simulation. Choosing a pore radius of 5.3 Å (dashed curve) resulted in a satisfactory agreement between the experimental data and the PNP-model.

Open channel probability

At steady state the channels flickered primarily between the main state and residual state. Hence, single-channel records allowed the determination of the probability of a channel's being in the main state, P_o. The pulse protocol involved the application of a V_j of long duration (20–30 s) and different amplitude. The initial segment of each I_j record was discarded to avoid interference from time-dependent inactivation and substates [28]. Figure 12A shows records gained with the K$^+$ aspartate$^-$ pipette solution. The currents were elicited by a V_j of 25 mV (top), 50 mV (middle) and 100 mV (bottom). They indicate that the dwell time at discrete levels is correlated with the amplitude of V_j. At 25 mV, the channel flickered rarely and was preferentially in the main state. At 50 mV, it flickered more frequently and spent less time in the main state and more time in the residual state. At 100 mV, it flickered rarely and was mainly in the residual state.

The records in Fig. 12A and others were used to assess P_o. The time in the main state was determined and divided by the record duration. The values of P_o were averaged and plotted vs. V_j (Fig. 12B). P_o decreased sigmoidally from 1 to 0 as V_j increased from 0 to 100 mV. The continuous curve represents the best fit of data to the Boltzmann equation using the following values: $V_{j,0}=40.6\pm1.9$ mV; $z=2.2\pm0.3$ (ten cell pairs; see Voltage dependence of gap junction currents). This $V_{j,0}$ is close to that obtained from the function $g_{j,ss}=f(V_j)$, i.e. 41.4 mV (see Table 1).
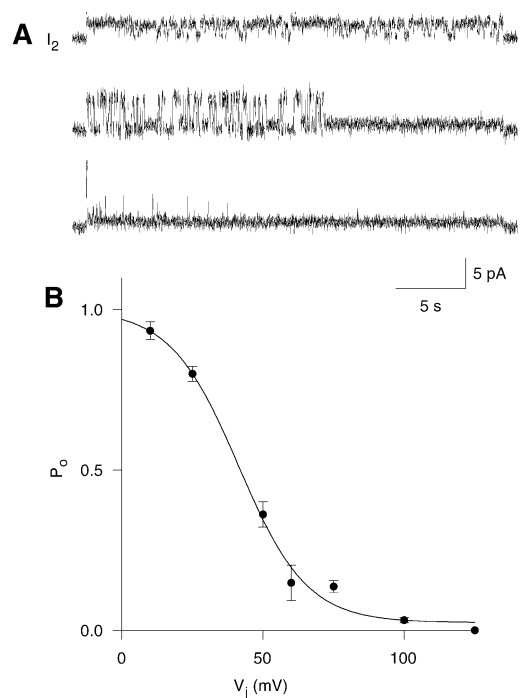

Fig. 12A, B Effects of V_j on probability of the channel open state, P_o. **A** Segments of I_j records from cell pairs with a single operational gap junction channel obtained at steady-state. Currents traces gained at $V_j=25$ mV (*top*), 50 mV (*middle*) and 100 mV (*bottom*). **B** Relationship between P_o and V_j. Values of P_o were determined from long-lasting records (20–30 s) during steady-state conditions. The *continuous curve* shows the best fit to the Boltzmann equation
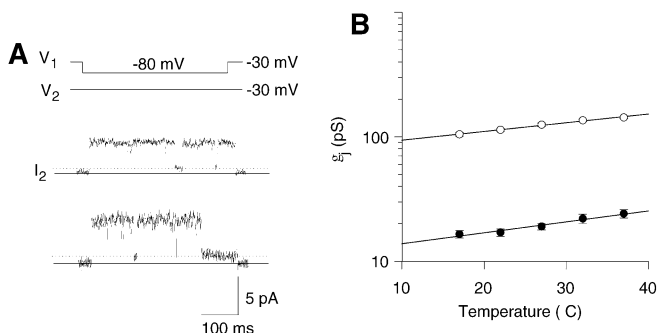
Influence of temperature on gap junction currents

To obtain further insight into the biophysical properties of Cx46 channels, the effect of temperature on I_j was examined with pipette solution containing K$^+$ aspartate$^-$. Figure 13A shows segments of continuous records gained at different temperatures. To determine $I_{j,inst}$ and $I_{j,ss}$, V_j pulses of 50 mV amplitude and 10 s duration were delivered to cell 1 and the currents displayed at expanded time scale. To monitor the transitions between temperatures, V_j pulses of 25 mV amplitude and 200 ms duration were applied and the signals presented on a compressed time scale.

At 17 °C (left-hand side), I_j inactivated slightly with time ($g_{j,inst}=1.23$ nS, $g_{j,ss}=0.75$ nS, $\tau_{i1}=1,100$ ms). At 37 °C (middle), it inactivated substantially due to disproportionate increases of $I_{j,inst}$ and $I_{j,ss}$ ($g_{j,inst}=1.77$ nS, $g_{j,ss}=0.48$ nS, $\tau_{i1}=256$ ms). Return to 17 °C (right hand side) led to a recovery ($g_{j,inst}=1.21$ nS, $g_{j,ss}=0.69$ nS, $\tau_{i1}=714$ ms). In five cell pairs, V_j was altered systematically to obtain a family of I_j records at 17 and 37 °C. Figure 13B summarizes the results. The ratios $g_{j,ss}/g_{j,inst}$ were averaged and plotted as functions of V_j. For clarity, only half of each data set is shown (positive V_j: 17 °C data; negative V_j: 37 °C data). The smooth curves represent the best fit of data to the Boltzmann equation
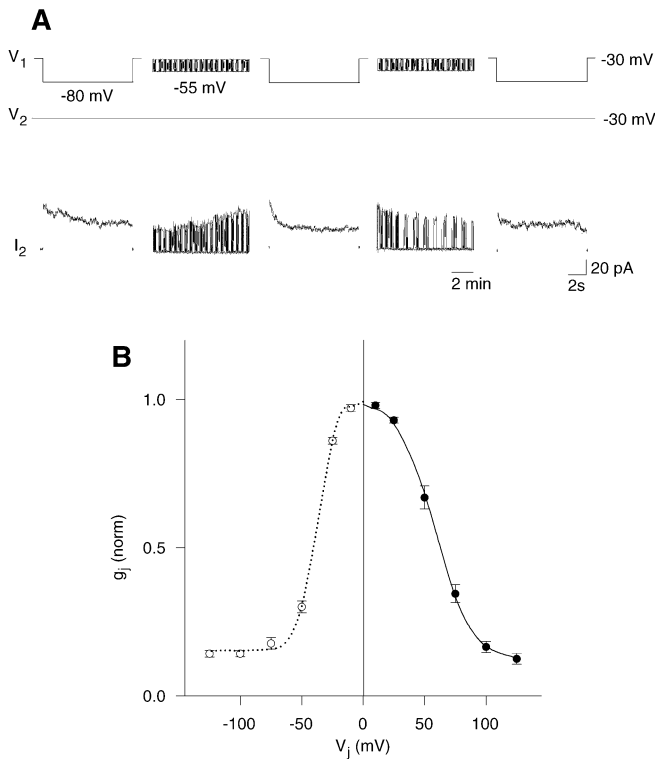
Fig. 13A, B Influence of temperature on multi-channel currents. **A** Segments of continuous records gained at 17 °C (*left*), 37 °C (*middle*) and 17 °C (*right*). To determine $I_{j,inst}$ and $I_{j,ss}$, long V_j pulses (10 s, 50 mV) were administered to cell 1. To monitor transitions between temperatures, short V_j pulses (200 ms, 25 mV) were applied. Note the different *time scale*. **B** Plot of normalized conductance at steady state, $g_{j,ss}$, vs. V_j. Data were obtained at 17 °C (●) and 37 °C (○). For clarity, only half of each data set is shown (five cell pairs each). The *smooth curves* show the best fits to Eq. 2. For the Boltzmann parameters, see text

Fig. 14A, B Influence of temperature on single-channel currents. **A** Responses of I_j to a V_j pulse of 50 mV and 300 ms (V_1=−80 mV, V_2=−30 mV) obtained at 17 °C (*upper trace*) and 37 °C (*lower trace*). The *continuous lines* indicate zero current, the *dotted lines* residual current. **B** Channel conductances $\gamma_{j,main}$ (○) and $\gamma_{j,residual}$ (●) on a logarithmic scale as functions of temperature. The *sloping lines* show the best fits to Eq. 12 using the temperature coefficients, Q_{10}, of 1.1 and 1.2, respectively

for following values: 17 °C: $V_{j,0}$=58.5 mV, $g_{j,min}$=0.12, z=1.7; 37 °C: $V_{j,0}$=38 mV, $g_{j,min}$=0.15, z=3.3.

These parameters and those obtained at 27 °C using the same pipette solution, i.e. K⁺ aspartate⁻ (see Table 1), were used to assess the temperature coefficient, Q_{10}, of the Boltzmann parameters. Averages of $V_{j,0}$, $g_{j,min}$ and z were plotted on a logarithmic scale vs. temperature (not shown). Over the range examined, i.e. 17–37 °C, each parameter increased with increasing temperature. The data were analysed using:

$$F_T = F_{17} \cdot Q_{10}^{\left[\frac{T-17}{10}\right]} \tag{12}$$

where T is the temperature in °C, F the parameter under investigation, and F_{17} the value of the parameter at the reference temperature, i.e. 17 °C. The best fit of data was obtained for the following Q_{10} values: 1.25, 1.2 and 1.38 for $V_{j,0}$, $g_{j,min}$ and z, respectively.

Figure 14A shows unitary currents recorded at different temperature. An increase from 17 to 37 °C (upper and lower I_2 trace) led to an increase in conductance, i.e. $\gamma_{j,main}$ increased from 104 to 143 pS and $\gamma_{j,residual}$ from 17 to 24 pS. This corresponds to a 1.38-fold and 1.41-fold increase, respectively. Figure 14B summarizes the results from 22 cell pairs including the data shown in Fig. 8B. Individual values of $\gamma_{j,main}$ (n=1,739) and $\gamma_{j,residual}$ (n=352) were averaged and plotted on a logarithmic scale vs. temperature. Over the range examined, i.e. 17–37 °C, $\gamma_{j,main}$ (open circles) and $\gamma_{j,residual}$ (solid circles) increased with increasing temperature. The solid lines represent the best fit of data to Eq. 12 using a Q_{10} of 1.1 and 1.2 for $\gamma_{j,main}$ and $\gamma_{j,residual}$, respectively.

Discussion

Our data indicate that rat Cx46 channels resemble other vertebrate gap junction channels, e.g. Cx30 [28], Cx40 [4] or Cx43 [27]. They exhibit several conductance states and are sensitive to V_j. We show that many of the basic electrical properties are dependent on the ionic composition of the pipette solution. Control solution containing K⁺ aspartate⁻ was used to mimic physiological conditions. During the interventions, these ions were replaced by TEA⁺ and/or Cl⁻.

Voltage gating of I_j

The g_j of Cx46 gap junctions is gated by V_j, but not by V_m (latter data not shown). With regard to V_j gating, the analysis furnished the relationships $g_{j,inst}=f(V_j)$ and $g_{j,ss}=f(V_j)$, which characterize the instantaneous and steady-state properties, respectively (see Fig. 1B). On the one hand, $g_{j,inst}$ decreased slightly with increasing V_j, leading to a moderate curvature of $g_{j,inst}=f(V_j)$. A comparison of Figs. 1B and 9 (pipette solution: K⁺ aspartate⁻) indicates that the relationships $g_{j,inst}=f(V_j)$ and $\gamma_{j,main}=f(V_j)$ resemble each other, suggesting that the

former reflects a genuine property of single channels. The $g_{j,inst}$ data were approximated considering an exponential relationship between the hemichannel conductance and V_j [23, 26, 33]. On the other hand, $g_{j,ss}$ decreased sharply with increasing V_j producing a symmetrical, bell-shaped function $g_{j,ss}=f(V_j)$ best described by two Boltzmann equations.

With pipette solution containing K^+ aspartate$^-$, the analysis of $g_{j,ss}$ data yielded the following Boltzmann parameters: $V_{j,0}=-42/42$ mV, $g_{j,min}=0.12/0.12$ and $z=2.5/2.5$ (negative/positive V_j; see Table 1). Replacing K^+ and aspartate$^-$ in the pipette solution by TEA^+ and/or Cl^- showed that intracellular ions affect $g_{j,min}$ and $V_{j,0}$, but not z (see Table 1). Substitution of the major charge carriers led to the sequence KCl>K^+ aspartate$^-$>TEA^+ Cl^->TEA^+ aspartate$^-$ for $g_{j,min}$. Moreover, there was a close match between $g_{j,min}$ and $\gamma_{j,residual}/\gamma_{j,main}$ for solutions with KCl (0.15 and 0.15), K^+ aspartate$^-$ (0.13 and 0.15), TEA^+ Cl^- (0.10 and 0.11) or TEA^+ aspartate$^-$ (0.07 and 0.09), i.e. $g_{j,min}$ and $\gamma_{j,residual}/\gamma_{j,main}$ follow the same ion sequence. Hence, the changes in $g_{j,min}$ are accounted for by alterations in $\gamma_{j,main}$ and $\gamma_{j,residual}$. Exchange of the pipette solution yielded the sequence KCl<K^+ aspartate$^-$<TEA^+ Cl^-≅TEA^+ aspartate$^-$ for $V_{j,0}$. Substitution of KCl for TEA^+ aspartate$^-$ provoked an increase in $V_{j,0}$ by 13–14 mV. Conceivably, this reflects a change in P_o. Examining Cx43 channels, we found similar effects on $V_{j,0}$ and $g_{j,min}$ caused by the pipette solutions [27].

The Boltzmann parameters obtained under quasi-physiological ionic conditions, i.e. pipette solution with K^+ aspartate$^-$, are similar to those reported for mouse lens fibre cells ($V_{j,0}=38.6$ mV, $g_{j,min}=0.11$, $z=2.2$) [9]. This may be fortuitous since fibre cells express both Cx46 and Cx50. Our data agree with those for rat Cx46 channels expressed in N2A cells ($V_{j,0}=48$ mV, $g_{j,min}=0.11$, $z=2$) [14], but deviate from those for mouse Cx46 expressed in *Xenopus* oocytes ($V_{j,0}=67$ mV, $g_{j,min}=0.1$, $z=2.2$ [37]; $V_{j,0}=66$ mV, $g_{j,min}=0.23$, $z=2$ [11]). The latter may reflect the lower temperature used, i.e. 20–22 °C. Our data obtained at 17 °C partially support this view ($V_{j,0}=58.5$ mV, $g_{j,min}=0.12$, $z=1.7$).

Kinetics of I_j inactivation

The inactivation of Cx46 channels is controlled by voltage. The larger V_j, the faster the inactivation of I_j. Hence, Cx46 channels behave like other Cx channels (e.g. [4, 27, 28]). In the presence of K^+ aspartate$^-$, I_j decreased as a single exponential for $V_j \leq 100$ mV (τ_{i1}) and as a sum of two exponentials for $V_j>100$ mV (τ_{i1} and τ_{i2}; see Fig. 3). Substitution of the pipette solution indicated that the kinetics of I_j inactivation are also affected by intracellular ions (see Figs. 5 and 6). In the presence of KCl, a second time constant was already evident at $V_j>75$ mV. With TEA^+ Cl^- and TEA^+ aspartate$^-$, τ_{i2} was not detectable up to $V_j \leq 125$ mV. Hence, the dissociation of τ_i into two components is emphasized by large V_j and small ions, i.e. I_j inactivates with a single time constant at

quasi-physiological conditions (K^+ aspartate$^-$ and small to moderate V_j). The functions $\alpha=f(V_j)$ and $\beta=f(V_j)$ derived from τ_{i1} data indicated that α is less voltage sensitive than β (see Figs. 4B and 6B and Table 2), i.e. $\alpha>\beta$ when $V_j<V_{j,0}$ and $\alpha<<\beta$ when $V_j>V_{j,0}$. Hence, at high V_j the conductance state of the channels is primarily determined by the closing rate constant.

Gap junction channels preferentially exhibit two conductance states, i.e. $\gamma_{j,main}$ and $\gamma_{j,residual}$. Since each channel consists of two hemichannels, hc1 and hc2, the 2 conductive states can be ascribed to three conformational states, hc1$_{high}$-hc2$_{high}$ and hc1$_{high}$-hc2$_{low}$ or hc1$_{low}$-hc2$_{high}$ [33]. Assuming first-order reactions between conformational states, the state machine predicts single time constants for I_j inactivation. Hence, this scheme seems to conflict with the observation of a second time constant. Whilst it is conceivable that, τ_{i2} may be an artefact caused by series resistance problems, this seems unlikely because cell pairs with $g_{j,inst}>2$ nS were discarded from the analysis. Alternatively, two time constants may exist, the slower one not always being resolvable. Adverse conditions for its detection include small currents and/or slow inactivation, situations prevailing at small V_j and/or in the presence of large ions. As far as the significance of τ_{i2} is concerned, several possibilities come to mind: (i) a second residual state, (ii) subconductance states, (iii) a closed state and (iv) electrostatic interaction between ions and the channel wall. With respect to (i), a fourth conformational state, hc1$_{low}$-hc2$_{low}$, may lead to a third conductive state (between $\gamma_{j,residual}$ and zero) and hence an extra time constant. However, simulation studies have shown that the probability of such a state is extremely low [33] and hence its effect may be negligible. With regard to (ii), substates have been observed preferentially early during V_j pulses (see also [28]). This would be consistent with the finding that dynamic (i.e. α and β) and steady-state data (i.e. $g_{j,ss}/g_{j,inst}$) reveal a different $V_{j,0}$ (compare Tables 1 and 2). With respect to (iii), it has been reported that the incidence of channel closed states increases with increasing V_j [1]. Hence, this possibility cannot be ruled out. With regard to (iv), charge separation during current flow may occur due to interactions between the ions and the channel wall. This would be consistent with the finding that small ions favour the presence of a second time constant.

Replacing the pipette solution showed that the relationship $\tau_{i1}=f(V_j)$ was also affected by the intracellular ions (see Fig. 6A). Replacing Cl^- by aspartate$^-$ increased τ_{i1}, irrespective of the cation. Likewise, replacing K^+ with TEA^+ also increased in τ_{i1}, irrespective of the anion. In other words, for τ_{i1} to reach a given value, V_j had to be increased when changing from KCl to K^+ aspartate$^-$, TEA^+ Cl^- and TEA^+ aspartate$^-$ solution. This shift along the V_j axis suggests that more energy is required for I_j inactivation in the presence of larger ions. This would be consistent with screening of surface charges of connexins and thereby altering of the electric field across the channels. These arguments are valid for voltages larger than 50 mV. At smaller voltages, there is considerable

disagreement between experimental and calculated values of τ_{i1}. This reflects the fact that τ_{i1} data were not only scarce but also inaccurate, especially in the case of large ions and small currents. The data also indicate that the increase of τ_{i1} in the presence of larger ions is caused by a decrease in β (see Fig. 6B). This was most prominent at larger V_j. There was virtually no change in α. Examining Cx43 channels and running computer simulations, we have made similar observations [29]. Conceivably, electrical interactions between ions and channel surface charges may affect the inactivation kinetics of I_j.

Published data on the kinetics of I_j inactivation are contradictory. Some investigators have reported a single time constant (amphibian blastomeres [13]; hamster Cx43 [34]; rat Cx32 [5]; human Cx45 [19]; mouse Cx30 [28]), others two (rat Cx40 [16]; zebrafish retina [18]). In rat Cx43, we have also found two time constants at $V_j > 100$ mV [29]. However, in this case τ_{i2} was more prominent in the presence of large ions (TEA$^+$ aspartate$^-$ vs. KCl). This may reflect differences in surface charge among connexin channels.

Kinetics of I_j restitution

The recovery of I_j from inactivation was studied in the presence of K$^+$ aspartate$^-$ solution. Its time course followed a single exponential resulting in the time constant τ_r (see Fig. 7). The behaviour of $\tau_r = f(V_j)$ and $\tau_i = f(V_j)$ was complementary. A small V_j gave rise to slow inactivation followed by fast recovery, and vice versa (compare Figs. 4 and 7). This behaviour offers an additional means of controlling the extent of functional coupling between adjacent cells, especially in the case of repetitive changes in V_j. This mechanism may be relevant in cardiac tissue, e.g. in the sinoatrial node since it expresses Cx46 and is prone to rhythmic changes [31].

Reports in the literature dealing with I_j recovery are scarce. An early study reported single exponentials with time constants identical to those of I_j inactivation (amphibian blastomeres [13]). Subsequent exploratory studies have yielded single exponentials with $\tau_r > \tau_i$ (hamster heart [34]; chicken heart [30]; bass retina [17]) and τ_r alone (rat Cx46 expressed in *Xenopus* oocytes [11]).

Single-channel properties

Cx46 channels exhibit several conductance states: a main state, several substates, a residual state and a closed state. The main and residual states were long lived while substates, interposed between the two, were short lived and hence difficult to study (see Fig. 8A). Closed states were seen in the presence of chemical uncouplers (e.g. heptanol; data not shown). Current transitions between channel open states were fast (<2 ms), those involving the closed state were slow (5–15 ms). The residual state explains the incomplete decline of g_j at large V_j (see

Figs. 1B and 2). These results are consistent with the current concept of gap junction channel operation [4, 27, 28]. Values of $\gamma_{j,main}$ and $\gamma_{j,residual}$ were determined under different conditions. Under quasi-physiological conditions (K$^+$ aspartate$^-$ solution; T=37 °C; extrapolated to $V_{j,0}$=0 mV), the predicted values are 152 and 28 pS, respectively. These values are comparable to those for rat Cx46 expressed in N2A cells (140 and 27 pS; pipette solution: CsCl) [14]. However, they deviate from those of lens fibre cells [9]. That study reported a γ_j histogram with three peaks (78, 136 and 207 pS; pipette solution: K$^+$ aspartate$^-$; T=22 °C), attributing the larger values to channels characteristic of fibre cells.

Detailed analysis revealed that $\gamma_{j,main}$ and $\gamma_{j,residual}$ are both sensitive to V_j, i.e. both decreased with increasing V_j (see Fig. 9). This is consistent with $g_{j,inst} = f(V_j)$ (see Fig. 1B). The γ_j data were fitted with an equation for homotypic channels assuming rectifying hemichannels [33]. This prediction has been verified in transfected HeLa cells [25, 26] and injected oocytes [23].

Our experiments also showed that the channel conductances depend on the ions in the pipette solution. Substituting solutions, we found that the sequence for $\gamma_{j,main}$ and $\gamma_{j,residual}$ are identical and match that for the conductivity of the pipette solution, σ: KCl>K$^+$ aspartate$^-$>TEA$^+$ Cl$^-$>TEA$^+$ aspartate$^-$ (see Table 3). Moreover, $\gamma_{j,residual}$ was more susceptible to changes in σ than $\gamma_{j,main}$ (see Fig. 11). This is also evident from the following observations: (i) the ratio $\gamma_{j,residual}/\gamma_{j,main}$ did not remain constant, i.e. it was 0.15, 0.15, 0.11 and 0.09 for the respective solutions; (ii) the ratio γ_j(TEA$^+$ aspartate$^-$)/γ_j(KCl) for the main state and residual state was 0.31 and 0.19, respectively. Hence, the residual state is a more prominent hindrance for ion transfer than the main state as previously reported for Cx43 channels [27]. Furthermore, the conductance data in Table 3 can be used to estimate relative selectivity ratios. A comparison of the $\gamma_{j,main}$ and $\gamma_{j,residual}$ data obtained with pipette solutions of *identical anions* leads to a mean ratio for K$^+$:TEA$^+$ of 1:0.51 and 1:0.36, respectively [procedure: average of $\gamma_{j,main}$(TEA$^+$ Cl$^-$)/$\gamma_{j,main}$(KCl) and $\gamma_{j,main}$(TEA$^+$ aspartate$^-$)/$\gamma_{j,main}$(K$^+$ aspartate$^-$), respectively average of $\gamma_{j,residual}$(TEA$^+$ Cl$^-$)/$\gamma_{j,residual}$(KCl) and $\gamma_{j,residual}$(TEA$^+$ aspartate$^-$)/$\gamma_{j,residual}$(K$^+$ aspartate$^-$)]. Conversely, a comparison of $\gamma_{j,main}$ and $\gamma_{j,residual}$ data gained with solutions of *identical cations* leads to a mean ratio for Cl$^-$:aspartate$^-$ of 1:0.6 and 1:0.55, respectively. This implies that K$^+$ passes more readily than TEA$^+$ through a channel in the main state and residual state, and Cl$^-$ more easily than aspartate$^-$. Moreover, the residual state impairs TEA$^+$ more effectively than aspartate$^-$. This is consistent with the view that Cx46 channels discriminate cations and anions on the basis of ionic rather than hydrated radii.

Our γ_j data alone do not allow absolute ionic selectivities to be deduced. Matrix calculations yield four equations of which only three are linearly independent. This is because the sum of cations and anions is invariant in each pipette solution. This problem can be approached considering the selectivity data of Cx46 hemichannels.

These channels reportedly prefer cations to anions (K^+:Cl^-=10:1) and obey the selectivity sequence Cs^+>K^+>Na^+>Li^+>TMA^+>TEA^+ (1.19:1.0:0.8:0.64:0.34: 0.2) [23, 32]. Using our $\gamma_{j,main}$ data and an equation specifying this K^+:Cl^- ratio, the calculated conductance contributed by aspartate$^-$ was negative, thus violating physico-chemical principles. Using our $\gamma_{j,main}$ data and the ratio K^+:TEA^+=1:0.2, we obtained the selectivity sequence K^+>Cl^->aspartate$^-$>TEA^+ (1.0:0.95:0.33:0.2). This suggests that Cx46 gap junction channels, unlike their hemichannels, exhibit no general preference for cations to anions. Instead, their ionic selectivity appears to be controlled by ionic size. Hence, docking of hemichannels may introduce structural modifications involved in setting the ionic selectivity of gap junction channels. However, this conclusion conflicts with a report claiming that the ionic selectivity of Cx46 hemichannels is maintained in Cx46 gap junction channels [24].

The open probability of Cx46 channels decreased with increasing V_j obeying a sigmoidal function P_o=$f(V_j)$ (see Fig. 12B). The analysis provided the following Boltzmann parameters (pipette solution: K^+ aspartate$^-$): $V_{j,0}$=41 mV, z=2. Hence, $g_{j,min}$ cannot be explained by a partial decrease in P_o (see Voltage gating of I_j). These values are consistent with those obtained from the relationship $g_{j,ss}$=$f(V_j)$ (see Table 1). For comparison, mouse Cx40 expressed in HeLa cells yield a similar $V_{j,0}$ value for P_o=$f(V_j)$ and $g_{j,ss}$=$f(V_j)$ data [4]. The same finding has been reported for rat Cx32 in Schwann cells [5]. However, in HeLa cells expressing mouse Cx30, $V_{j,0}$ gained from P_o data is significantly larger than that from $g_{j,ss}$ data [28]. This has been explained by interactions among channels, an effect which may be connexin specific.

PNP-model simulations

The PNP-model was originally developed to describe ion channels in isolated cells [7]. Recently, it has also been applied to gap junction channels and hemichannels [24]. With our own $\gamma_{j,main}$ data gained with K^+ aspartate$^-$ solution, it was possible to model the conductance and the rectification of a Cx46 gap junction channel by placing negative charges close to the intracellular endings (see Fig. 9). This behaviour of the model ensues from the different diffusion properties of the ion species. However, according to the model this charge profile predicts outward rectification for a Cx46 hemichannel (data not shown), a property which contradicts with the experimental observations [23, 24]. Moreover, irrespective of the fixed charge distribution, the PNP-model does not show rectification for homotypic gap junction channels in the presence of solutions with small ions of similar diffusion coefficients, e.g. K^+ and Cl^- (data not shown). While this behaviour seems to be consistent with two recent reports [17, 24], it conflicts with our own observations (R. Sakai, R. Weingart, unpublished results). The discrepancies between our measurements and PNP-

simulations may arise from the fact that the application of the PNP-model to gap junction channels does not take into account the structural and electrical properties of the docking zone. Specifically, putative effects of the extracellular bulk potential on the potential profile and the conductive behaviour are not considered. Furthermore, a fit of our data required a pore radius of 5.3 Å rather than the 4.75 Å previously proposed for Cx46 gap junction channels [24]. This discrepancy may reflect the effects of hemichannel docking on channel conductance [24]. Using the channel parameters deduced from the K^+ aspartate$^-$ solution data, PNP-modelling yielded the same solution-dependent ranking of $\gamma_{j,main}$ as our experiments. However, while the values for the solutions containing aspartate$^-$ were identical (K^+ aspartate$^-$: 127 vs. 127.5 pS; TEA^+ aspartate$^-$: 66 vs. 65.7 pS; see Table 3), they deviated for Cl^- containing solutions (KCl: 157 vs. 212.7 pS; TEA^+ Cl^-: 81 vs. 108.8 pS). This suggests that each pipette solution is longing for another charge distribution. These considerations indicate that the PNP-model predicts some aspects of the electrical properties of gap junction channels, but not all.

Temperature effects

Elevation of temperature increased the conductances and accelerated the kinetics at both single- and multi-channel levels (see Figs. 13 and 14). With regard to single-channel properties, the Q_{10} for $\gamma_{j,main}$ and $\gamma_{j,residual}$ was 1.1 and 1.2, respectively (temperature range: 17–37 °C). This is consistent with the view that ion transfer in the residual state is impaired slightly compared with the main state. Steric and/or electrical constrains may be responsible. The same conclusion has been drawn from studies on Cx30 and Cx40 channels [4, 28]. With regard to multi-channel properties, increasing the temperature decreased $V_{j,0}$ and increased $g_{j,min}$ and z. The Q_{10} values were 1.3, 1.2 and 1.4, respectively, i.e. slightly above that for pure physical processes. The increase in $g_{j,min}$ is compatible with the increase in γ_j. It may relate to an increase in σ and conformational changes of the channel proteins. The latter may be responsible for the increase in z.

Significance for the physiological role of Cx46

The results presented yield a deeper insight into the properties of Cx46 channels. The unitary conductance is rather large. It suggests a considerable pore size, a property beneficial to the metabolism in the avascular lens. Early during cataractogenesis, the fibre cells of the lens swell and form pinhead opacities containing elevated levels of Ca^{2+} sufficient to close gap junction channels [10]. Rupture of the membrane of swollen fibre cells leads to depolarization of V_m creating a voltage drop between ruptured and intact cells, while the Ca^{2+} level increases in the damaged cells. As a result, V_j gating and Ca^{2+} gating of Cx46 channels begin to operate and may play a

defensive role by restricting opacification to discrete regions.

References

1. Banach K, Weingart R (2000) Voltage gating of Cx43 gap junction channels involves fast and slow current transitions. Pflugers Arch 439:248–250
2. Beyer EC, Kistler J, Paul DL, Goodenough DA (1989) Antisera directed against connexin43 peptides react with a 43-kD protein localized to gap junctions in myocardium and other tissues. J Cell Biol 108:595–605
3. Bukauskas FF, Weingart R (1993) Voltage-dependent gating of single gap junction channels in an insect cell line. Temperature dependence of gap junction properties in neonatal rat heart cells. Pflugers Arch 423:133–139
4. Bukauskas FF, Elfgang C, Willecke K, Weingart R (1995) Biophysical properties of gap junction channels formed by mouse connexin40 in induced pairs of transfected human HeLa cells. Biophys J 68:2289–2298
5. Chanson M, Chandross KJ, Rook MB, Kessler JA, Spray DC (1993) Gating characteristics of a steeply voltage-dependent gap junction channel in rat Schwann cells. J Gen Physiol 102:925–946
6. Chen C, Okayama H (1987) High efficiency transformation of mammalian cells by plasmid DNA. Mol Cell Biol 7:2745–2753
7. Chen DP, Xu L, Tripathy A, Meissner G, Eisenberg B (1999). Selectivity and permeation in calcium release channel of cardiac muscle: alkali metal ions. Biophys J 76:1346–1366
8. Donaldson PJ, Roos M, Evans C, Beyer E, Kistler J (1994) Electrical properties of mammalian lens epithelial gap junction channels. Inv Ophthalm Vis Sci 35:3422–3428
9. Donaldson PJ, Dong Y, Roos M, Green C, Goodenough DA, Kistler J (1995) Changes in lens connexin expression lead to increased gap junctional voltage dependence and conductance. Am J Physiol 269:C590–C600
10. Duncan G, Williams M R, Riach RA (1994) Calcium, cell signalling and cataract. Progr Ret Eye Res 13:623–652
11. Ebihara L, Berthoud VM, Beyer EC (1995) Distinct behavior of connexin56 and connexin46 gap junctional channels can be predicted from the behavior of their hemi-gap-junctional channels. Biophys J 68:1796–1803
12. Goodenough DA (1992) The crystalline lens. A system networked by gap junctional intracellular communication. Semin Cell Biol 3:49–58
13. Harris AL, Spray DC, Bennett MVL (1981) Kinetic properties of a voltage-dependent junctional conductance. J Gen Physiol 77:95–117
14. Hopperstad MG, Srinivas M, Spray DC (2000) Properties of gap junction channels formed by Cx46 alone and in combination with Cx50. Biophys J 79:1954–1966
15. Horst M, Harth N, Hasilik A (1991) Biosynthesis of glycosylated human lysozyme mutants. J Biol Chem 266:13914–13919
16. Lal R, Arnsdorf MF (1992) Voltage-dependent gating and single-channel conductance of adult mammalian atrial gap junctions. Circ Res 71:737–743
17. Lu C, McMahon DG (1996) Gap junction channel gating at bass retinal electrical synapses. Vis Neurosci 13:1049–1057
18. McMahon DG, Brown DR (1994) Modulation of gap-junction channel gating at Zebrafish retinal electrical synapses. J Neurophysiol 72:2257–2268
19. Moreno AP, Laing JG, Beyer EC, Spray DC (1995) Properties of gap junction channels formed of connexin 45 endogenously expressed in human hepatoma (SKHep1) cells. Am J Physiol 268:C356–C365
20. Musil LS, Beyer EC, Goodenough DA (1990) Expression of the gap junction protein connexin43 in embryonic chick lens: molecular cloning, ultrastructual localization, and post-translational phosphorylation. J Membr Biol 116:163–175
21. Paul DL, Ebihara L, Takemoto LJ, Swenson KI, Goodenough DA (1991) Connexin46, a novel lens gap junction protein, induces voltage-gated currents in nonjunctional plasma membrane of *Xenopus* oocytes. J Cell Biol 115:1077–1089
22. Sakai R, Elfgang C, Willecke K, Weingart R (1998) Electrical properties of rat Cx46 gap junction channels studied in transfected HeLa cells (abstract). Pflugers Arch 435:R47
23. Trexler EB, Bennett MVL, Bargiello TA, Verselis VK (1996) Voltage gating and permeation in a gap junction hemichannel. Proc Natl Acad Sci USA 93:5836–5841
24. Trexler EB, Bukauskas FF, Kronengold J, Bargiello TA, Verselis VK (2000) The first extracellular loop domain is a major determinant of charge selectivity in connexin46 channels. Biophys J 79:3036–3051
25. Valiunas V, Weingart R (1997) Voltage gating and conductive properties of gap junction hemichannels studied in transfected HeLa cells. In: Proceedings of the 1997 International Gap Junction Conference, Key Largo, Florida, USA, July 12–17, 1997, p 97
26. Valiunas V, Weingart R (2000) Electrical properties of gap junction hemichannels identified in transfected HeLa cells. Pflugers Arch 440:366–379
27. Valiunas V, Bukauskas FF, Weingart R (1997) Conductances and selective permeability of connexin43 gap junction channels examined in neonatal rat heart cells. Circ Res 80:708–719
28. Valiunas V, Manthey D, Vogel R, Willecke K, Weingart R (1999) Biophysical properties of mouse connexin30 gap junction channels in transfected human HeLa cells. J Physiol (Lond) 519:631–644
29. Valiunas V, Vogel R, Weingart R (2000) The kinetics of gap junction currents are sensitive to the ionic composition of the pipette solution. Pflugers Arch 440:835–842
30. Veenstra RD (1990) Voltage-dependent gating of gap junction channels in embryonic chick ventricular rat heart cells. Am J Physiol 258:C662–C672
31. Verheule S, van Kempen MJA, Postma S, Rook MB, Jongsma HJ (2001) Gap junctions in the rabbit sinoatrial node. Am J Physiol 280:H2103–H2115
32. Verselis VK, Trexler EB, Bukauskas FF (2000) Connexin hemichannels and cell-cell channels: comparison of properties. Braz J Med Biol Res 33:379–389
33. Vogel R, Weingart R (1997) Mathematical model of vertebrate gap junctions derived from electrical measurements on homotypic and heterotypic channels. J Physiol (Lond) 510:177–189
34. Wang H-Z, Li J, Lemanski LF, Veenstra RD (1992) gating of mammalian cardiac gap junction channels by transjunctional voltage. Biophys J 63:139–151
35. Wilders R, Jongsma HJ (1992) Limitations of the dual voltage-clamp method in assaying conductance and kinetics of gap junction channels. Biophys J 63:942–953
36. White TW, Bruzzone R, Goodenough DA, Paul DL (1992) Mouse Cx50, a functional membrane of the connexin family of gap junction proteins, is the lens fiber protein MP70. Mol Biol Cell 3:711–720
37. White TW, Bruzzone R, Wolfram S, Paul DL, Goodenough DA (1994) Selective interaction among the multiple connexin proteins expressed in vertebrate lens: The second extracellular domain is a determinant of compatibility between connexins. J Cell Biol 125:879–892